

A RECONNECTION-DRIVEN RAREFACTION WAVE MODEL FOR CORONAL OUTFLOWS

S. J. BRADSHAW¹, G. AULANIER², AND G. DEL ZANNA³

¹ Department of Physics and Astronomy, Rice University, Houston, TX 77005, USA; stephen.bradshaw@rice.edu
² LESIA, Observatoire de Paris, CNRS, UPMC, Université Paris Diderot, 5 place Jules Janssen, 92190 Meudon, France
³ DAMTP, Centre for Mathematical Sciences, Wilberforce Road, Cambridge, CB3 0WA, UK
Received 2011 June 13; accepted 2011 September 5; published 2011 November 22

ABSTRACT

We conduct numerical experiments to determine whether interchange reconnection at high altitude coronal null points can explain the outflows observed as blueshifts in coronal emission lines at the boundaries between open and closed magnetic field regions. In this scenario, a strong, post-reconnection pressure gradient forms in the field-aligned direction when dense and hot, active region core loops reconnect with neighboring tenuous and cool, open field lines. We find that the pressure gradient drives a supersonic outflow and a rarefaction wave develops in both the open and closed post-reconnection magnetic field regions. We forward-model the spectral line profiles for a selection of coronal emission lines to predict the spectral signatures of the rarefaction wave. We find that the properties of the rarefaction wave are consistent with the observed velocity versus temperature structure of the corona in the outflow regions, where the velocity increases with the formation temperature of the emission lines. In particular, we find excellent agreement between the predicted and observed Fe XII 195.119 Å spectral line profiles in terms of the blueshift (10 km s⁻¹), full width at half-maximum (83 mÅ) and symmetry. Finally, we find that $T_i < T_e$ in the open field region, which indicates that the interchange reconnection scenario may provide a viable mechanism and source region for the slow solar wind.

Key words: solar wind – Sun: corona

1. INTRODUCTION

The solar corona is a highly dynamic environment. EUV imaging and spectroscopy have revealed ubiquitous plasma flows within active regions (ARs). For example, *Transition Region and Coronal Explorer (TRACE)* EUV images show apparent flows in large, warm (1 MK) coronal loops (Schrijver et al. 1999; Winebarger et al. 2001), which are also seen by *SDO-AIA*. EUV imaging provides high cadence and high spatial resolution, but the interpretations of the observations can be ambiguous. For example, Wang et al. (2011) and Verwichte et al. (2010) find that these observations can also be consistent with slow magnetoacoustic waves. EUV spectroscopic observations made with *Hinode-EIS* have undoubtedly shown the presence of flows through the measurement of Doppler-shifted spectral emission line profiles. In this paper, we focus on the coronal outflows observed in blueshifted lines formed above 1 MK, at specific locations at the boundaries of the hot core loops in ARs.

The observed coronal outflows have a number of general properties as found by Del Zanna (2007, 2008) (also see Brooks & Warren 2011; Warren et al. 2011; Baker et al. 2009; Del Zanna & Bradshaw 2009; Doschek et al. 2008, 2007; Hara et al. 2008). Briefly, they (1) are stronger with increasing temperature above 1 MK, (2) are located above regions of strong magnetic field (sunspot umbrae and plage), (3) extend from very low to high altitudes, (4) are found in regions where the local electron density is much smaller (up to 2 orders of magnitude) than the characteristic densities of hot loops in AR cores, (5) are associated with non-thermal broadenings in the line profiles that exceed 50 km s⁻¹ and (6) are persistent and long-lived (for periods of days).

The mechanism driving these outflows is not yet known, though developing an understanding of their onset, morphology, and properties is extremely important for two reasons: (1) the outflows are potentially a manifestation of the process by which

the closed corona acquires its mass and energy; and (2) the outflows are the possible origin of the slow solar wind in open field regions (Brooks & Warren 2011; Doschek et al. 2008; Hara et al. 2008; Harra et al. 2008; Marsch et al. 2008).

In a recent paper, Baker et al. (2009) found that coronal upflows are related to the topology of the coronal magnetic field. They suggested four possible reconnection-related physical mechanisms to explain the flows. After further analysis Del Zanna et al. (2011) proposed more specifically that coronal outflows are due to interchange reconnection between high-pressure, closed loops in AR cores and adjacent low-pressure, open flux tubes. In their scenario, continuous AR expansion drives steady magnetic reconnection across separatrices at null points high in the corona, thus resulting in strong pressure gradients along the newly reconnected open and closed field lines. They conjectured that these pressure gradients lead to plasma outflows through the development of a rarefaction wave ($\partial v / \partial s > 0$, where v is the bulk flow velocity and s is the field-aligned coordinate).

In the current work, we investigate the plausibility of this mechanism by quantifying its effect both on the plasma and EUV radiation. First, we determine the post-reconnection evolution of the plasma through one-dimensional (1D) numerical radiative-hydrodynamic models of both the open and closed field cases. Next, we use our numerical results to forward-model the spectral properties of emission lines across a range of coronal temperatures in order to make quantitative predictions for direct comparison with *Hinode-EIS* spectral data. As far as we have been able to ascertain, we present the first full hydrodynamic model, including nonequilibrium ionization of the plasma evolution along reconnected magnetic field lines in the solar corona.

In Section 2 we describe our model, in Section 3 we discuss our results for outflows in open and closed field regions, and in Section 4 we summarize our findings and present a number of conclusions.

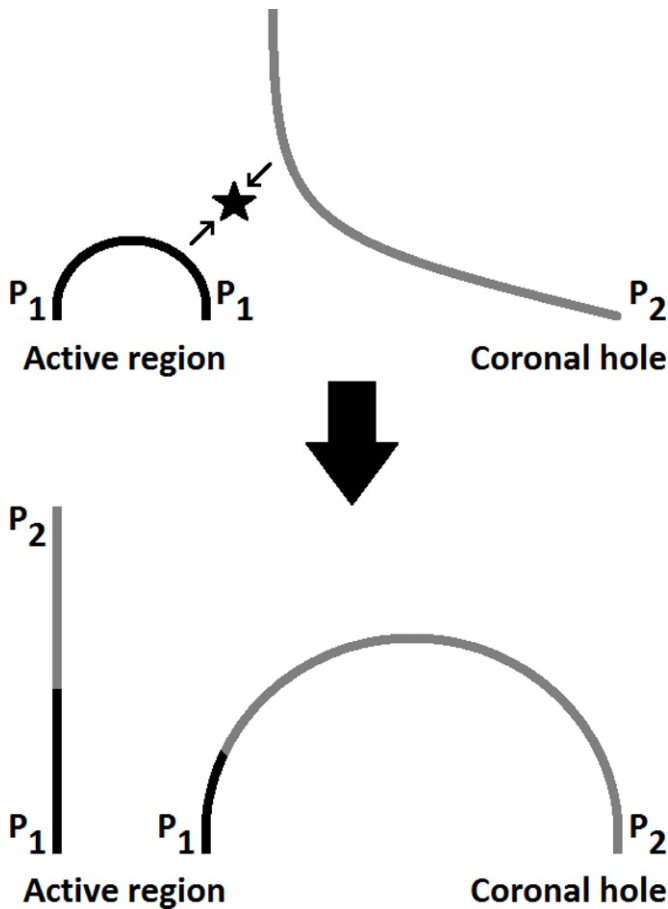


Figure 1. Magnetic reconnection takes place between neighboring closed (black) and open (gray) field lines at a high altitude null point in the corona (top). $P_1 > P_2$ leading to rarefaction waves and outflows in the newly reconnected open and closed field regions (bottom).

2. NUMERICAL MODEL AND EXPERIMENTS

We base our numerical model on the concept presented in Figure 10 of Del Zanna et al. (2011). The hot, dense loops at the core of an AR reconnect at a high-altitude coronal null point with the open field lines of a surrounding coronal hole, where the plasma is significantly cooler and more tenuous. New loops and open field regions are then created with strong field-aligned pressure gradients, leading to the formation of rarefaction waves and strong outflows. Figure 1 shows a conceptual view of the pre- and post-reconnection magnetic field geometry. The evolution of the magnetic field prior to reconnection is undoubtedly critical to its restructuring, but the post-reconnection evolution of the plasma is predominantly in the field-aligned direction ($\beta \ll 1$) and may therefore be treated as a 1D hydrodynamic system. We are primarily interested in determining the spectral characteristics of the outflows for comparison with observational data and the detailed treatment of the plasma permitted by 1D hydrodynamic modeling makes it ideally suited to this task.

In order to construct initial conditions describing the above scenario that are suitable for input to a 1D hydrodynamic model we adopt the following procedure to find the temperature, density, and pressure profiles along the newly formed field lines. We take $t = 0$ s as the time immediately following reconnection and solve the hydrostatic equations for (1) a uniformly heated, closed loop of length $L = 200$ Mm and

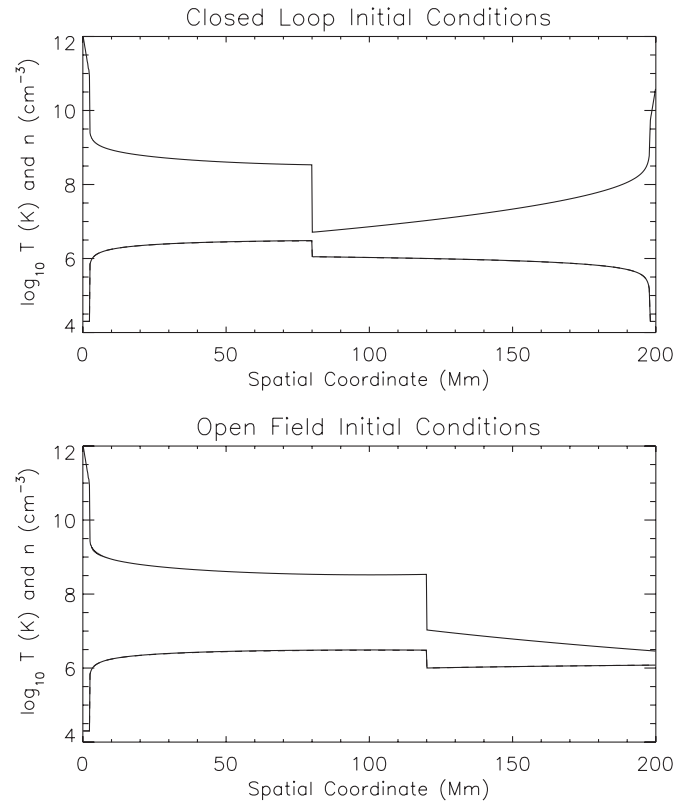


Figure 2. Field-aligned temperature and density profiles, immediately following reconnection, for the open and closed field cases.

peak temperature $T_{\text{apex}} = 3$ MK; and (2) uniform heating along an open field line of length $L = 200$ Mm and peak temperature $T = 1.2$ MK. Uniform heating in this case refers to uniform volumetric heating in the field-aligned direction. The field-aligned gravitational acceleration in (1) describes a semi-circular coronal loop normal to the solar surface ($g_{\parallel}(s=0) = g_{\odot}$ and $g_{\parallel}(\text{apex}) = 0$) and in (2) it describes a radial magnetic field line ($g(s=r) \propto 1/r^2$, where r is the radial distance).

The initial conditions for the newly reconnected closed loop are then generated by combining solution (1) for $s > 120$ Mm with solution (2) for $s \leq 120$ Mm, thus creating a new loop of length $L = 200$ Mm. In this way, solution (1) for $s > 120$ Mm is mapped onto the new loop for $0 < s < 80$ Mm and solution (2) for $s \leq 120$ Mm is mapped onto the new loop for $s \geq 80$ Mm.

The initial conditions for the newly reconnected open field line are generated by combining solution (1) for $s \leq 120$ Mm with solution (2) for $s > 120$ Mm, thus creating a new open field line of length $L = 200$ Mm. The resulting temperature and density profiles along the field for both the closed and open cases are shown in Figure 2.

In reality, the pre-reconnection core loops and coronal hole plasma are unlikely to be in hydrostatic equilibrium. However, the consequences of the kick to the system provided by the strong pressure gradients that form in the newly reconnected loops and open field regions are likely to dominate any pre-existing dynamical behavior. Since we are interested in the evolution of the plasma subject only to the pressure gradients, we apply their original uniform volumetric heating to the separate parts of solutions (1) and (2) that comprise the new closed loops and open field. This ensures that the plasma far from the reconnection site

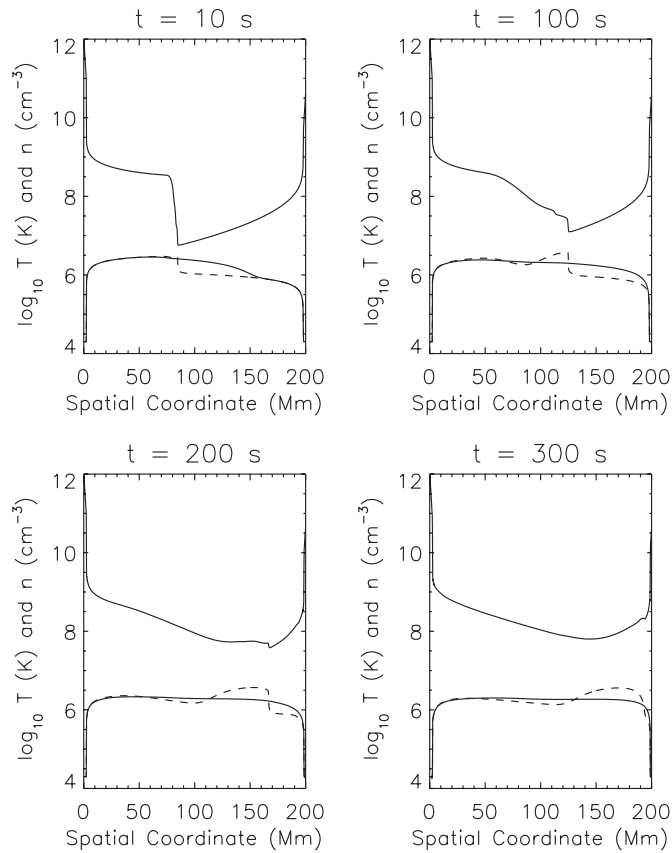


Figure 3. Field-aligned temperature and density profiles at selected times during the development of the rarefaction wave in the closed loop case. Number density (solid), electron temperature (solid), and ion temperature (dashed).

remains in hydrostatic equilibrium and responds only when it is reached by a propagating disturbance that originated at the reconnection site.

Clearly, the initial conditions shown in Figure 2 are far from hydrostatic equilibrium and so we follow the evolution of the plasma for $t > 0$ s by solving the system of hydrodynamic equations for the conservation of mass and momentum, together with separate equations for the electron and ion energies. Given the combination of high temperatures and low densities that arise in the initial conditions, we expect an electron heat front to propagate ahead of the material/ion front, which will drive the electron temperature up in the low-density regions where thermal equilibration timescales are longer than the timescale for the dynamical evolution of the plasma. The electron and ion temperatures quickly become decoupled and do not equilibrate even at relatively late times, thereby necessitating a two-fluid treatment of the plasma. This is shown in Figure 3. We also expect similar considerations to affect the ionization state of the plasma, which is dominated by collisions in the solar corona. The combination of a quickly changing electron temperature and low collision frequencies may drive the ionization state far from equilibrium, and consequently alter the properties of the emission spectrum. Our spectral modeling must account for this and we therefore solve the time-dependent ionization equations for Fe (the dominant emitting element in the corona) concurrently with the hydrodynamic equations in order to determine the population fraction of the coronal Fe ions as the plasma evolves. We use the HYDRAD code to perform the numerical experiments for the closed and open field cases.

The equations solved by HYDRAD and the code itself are described in detail in Bradshaw & Klimchuk (2011), and references therein. However, we will briefly discuss the aspects of HYDRAD that are directly relevant to the numerical experiments that we conduct in the present work. The boundaries for the closed loop case are deep (several scale heights) chromospheres at each footpoint, which are necessary for stability and to provide a source (sink) of mass and energy for the corona in the event of heating (cooling). Mass and energy loss by transport (bulk flows and conduction) through the very bottom of the chromospheres is prevented by the implementation of solid-wall boundary conditions ($v = 0$, isothermal temperature profile). The depth of the chromospheres ensures that any undue numerical influences through this choice are kept far away from the regions of interest in the computational domain. A variable cross-section for the flux tube (closed loop or open field) can be accounted for by the hydrodynamic equations through the inclusion of an area factor in the flux terms. We have chosen to maintain a constant cross-section, which we believe is acceptable for two reasons. (1) Adding an area expansion factor introduces extra parameters into our model for which we are uncertain of their values. We do not know whether the coronal magnetic field under the circumstances we are investigating is near potential, or best described by a linear/nonlinear force-free extrapolation from the photospheric field, for example. In the absence of such information we prefer clarity over extra detail. (2) We expect the essential physics to be unaffected. A rarefaction wave driven by a pressure gradient will arise in either circumstance (constant cross-section or expanding field). It may be the case that the properties of the wave might be somewhat affected, but we expect any differences to be small and for the qualitative properties of the wave to remain the same.

Since HYDRAD was originally developed to model closed loop systems, a modification to the upper boundary condition was necessary in order to handle the open field aspect to this work (the lower boundary is the same as in the closed loop case). Open boundary conditions are implemented using the ghost cell method (MacNeice et al. 2000), where cells placed just beyond the outer edge of the computational domain (ghost cells) are used to calculate quantities (such as gradients) at the inner edge. A geometric limiter (van Leer 1979; Centrella & Wilson 1984) is used to ensure that no overshoots in the conserved variables can be introduced at the boundary, which could otherwise lead to unphysical changes in these quantities, artificially steep gradients (and consequently strong forces and fluxes) and the possible onset of instabilities.

There is an important caveat to accurately modeling the evolution of plasma along open field lines in the case of gravitational stratification ($g \propto 1/r^2$). If a perturbation (such as a pressure imbalance) leads to the generation of a wind, then the wind will have the following properties: (1) if the sonic point falls within the computational domain then the classical Parker transonic (slow) wind develops; (2) if the sonic point falls outside the domain then an unphysical wind eventually develops, with a velocity that reaches the sound speed (C_s) at the top of the domain. These two solutions correspond to attractors in the classical $M-r$ phase plane. In the latter case, waves propagate back into the domain and have the effect of increasing the velocity at lower altitudes in order to match the attractor that is one of the Parker solutions between the upward and downward transonic curves in the low altitude region of the $M-r$ phase plane. This outflow solution corresponds to a breeze, which is an unstable flow structure and collapses into its symmetrical

($M \rightarrow -M$) critical inflow (accretion) profile. Therefore, one must be careful in the case of (2) that any conclusions are based upon solutions obtained well before the unphysical, asymptotic flow develops. Details concerning these issues can be found in Parker (1958), Velli (1994), and Del Zanna et al. (1998).

To forward-model the spectral properties of the coronal emission lines of interest we follow the line synthesis procedure described by Taroyan et al. (2006). However, we also fold the calculated intensities through the wavelength-resolved *Hinode*-EIS response functions and take account of instrumental broadening when calculating the line widths, which allows a direct comparison with observed emission line intensities. The instrument width for the short wavelength channel of EIS is 60 mÅ and 67 mÅ for the long wavelength channel (G. Del Zanna 2011, in preparation). See Section 3 of Bradshaw & Klimchuk (2011) for a full description of the forward-modeling procedure that we employ.

3. RESULTS

3.1. Closed Loop

Figure 3 shows the post-reconnection ($t > 0$ s) evolution of the field-aligned number density, electron (T_e) and ion (T_i) temperatures for the closed loop case. It can be seen that even after 300 s the electron and ion temperatures have not collisionally equilibrated. The reason for this is clear from the temperature profiles at $t = 10$ s in the top left panel of Figure 3, which show the electron thermal conduction front propagating far ahead of the ion front, and the density profile at $t = 300$ s, which shows values of order 10^8 cm $^{-3}$ and lower in the regions where $T_e \neq T_i$, implying long collision timescales. This justifies our use of the two-fluid approach and would lead to spectral line widths in these regions different to those calculated assuming that $T_e = T_i$; such a discrepancy may be amenable to observational verification. Figure 4 shows the evolution of the field-aligned velocity ($v = 0$ km s $^{-1}$ at $t = 0$ s) and Mach number. The initial pressure gradient is sufficient to drive supersonic upflows at all times, with a constant maximum Mach number of 1.5. A rarefaction wave is clearly evident and we consider it fully developed when it reaches the left-hand footpoint at $t = 300$ s. At this time the rarefaction wave extends from $s \approx 0$ Mm to about 130 Mm along the loop. Therefore, our numerical experiment confirms the development of a rarefaction wave, along the closed loop, in the scenario proposed by Del Zanna et al. (2011). Movies of Figures 3 and 4 are available from the authors.

We now turn our attention to determining the spectral properties of the rarefaction wave. A number of coronal emission lines are forward-modeled in order to predict how such a wave would be observed by *Hinode*-EIS. We assume a viewing geometry such that the loop is located at the solar disk center and oriented perpendicular to the solar surface; the instrument line of sight then lies in the plane of the loop. The emission along the loop for each spectral line is then binned into a single row of EIS pixels and so the spectrum in each pixel is the line-of-sight (for that pixel) integrated spectrum (see Figure 1 of Bradshaw & Klimchuk 2011). We choose a loop width equal to a single EIS pixel ($1'' \approx 760$ km) and take account of the increasing line-of-sight depth away from the apex, toward the footpoints. The line intensities can be scaled to other loop widths by following the procedure described in Section 5 of Bradshaw & Klimchuk (2011). The forward-modeling is carried out on the profiles of

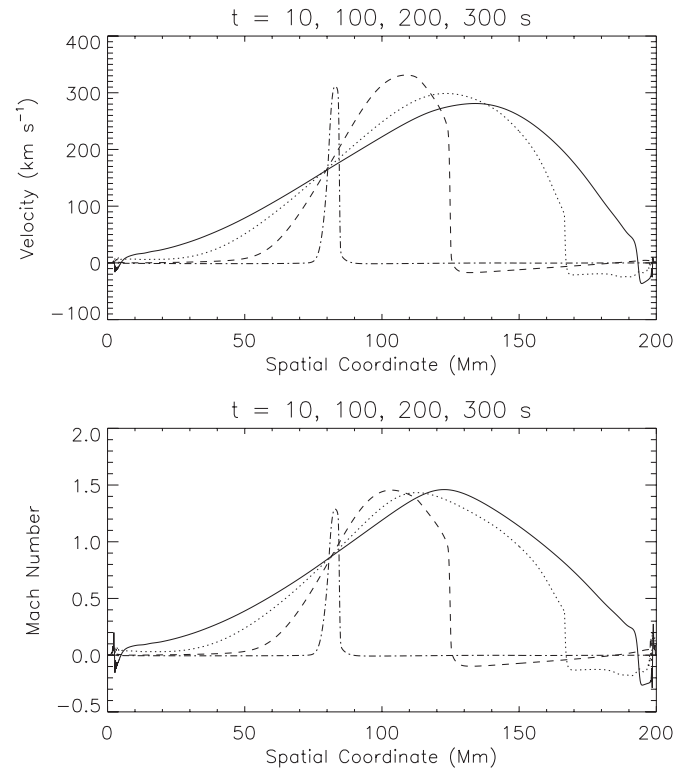


Figure 4. Field-aligned velocity and Mach number profiles at selected times during the development of the rarefaction wave in the closed loop case. 10 s (dash-dotted), 100 s (dashed), 200 s (dotted), and 300 s (solid).

the fully developed rarefaction wave at $t = 300$ s in Figures 3 and 4.

The left-hand column of Figure 5 contains a series of stack plots showing the relative intensity (normalized to the peak intensity) along the closed loop for several coronal emission lines that fall within the wavelength sensitivity range of EIS. Each stack plot begins at the left-hand footpoint, in the center of the first pixel (at $0''.5$, since each EIS pixel is $1''$), and each overlying curve shows the spectral line profile in the next pixel. For example, in the case of Fe x (184.537 Å) the emission along the line-of-sight peaks in the first pixel (covering the left-hand footpoint of the closed loop) and is negligible in subsequent pixels. The right-hand column of Figure 5 shows the spectral line profile and EIS count rates (instrument units) for the pixel corresponding to the peak emission in the neighboring stack plot. For example, in the case of Fe x (184.537 Å) the spectral line profile is for the first pixel.

The stack plots in Figure 5 show the velocity increasing along the loop (as expected from Figure 4) by the increasing Doppler-shift for Fe xii to Fe xvi. The variation in the angle between the field-aligned flow and the line of sight is taken into account. Negative velocities indicate a blueshift and therefore an upflow. The spectral line profiles in the right-hand column of Figure 5 also show that the upflow speed increases with temperature for the pixels in which the measured intensity is strongest. The blueshift is greater for higher charge states of Fe. Outflow speeds of < 5 km s $^{-1}$ are predicted for Fe x, 10 km s $^{-1}$ for Fe xii, 10–20 km s $^{-1}$ for Fe xiv, and 20–30 km s $^{-1}$ for Fe xvi. The spectral line profiles have been plotted for equilibrium and nonequilibrium ionization states to determine what impact this may have on the line intensities. At $t = 300$ s the ionization state is clearly near equilibrium in the cooler

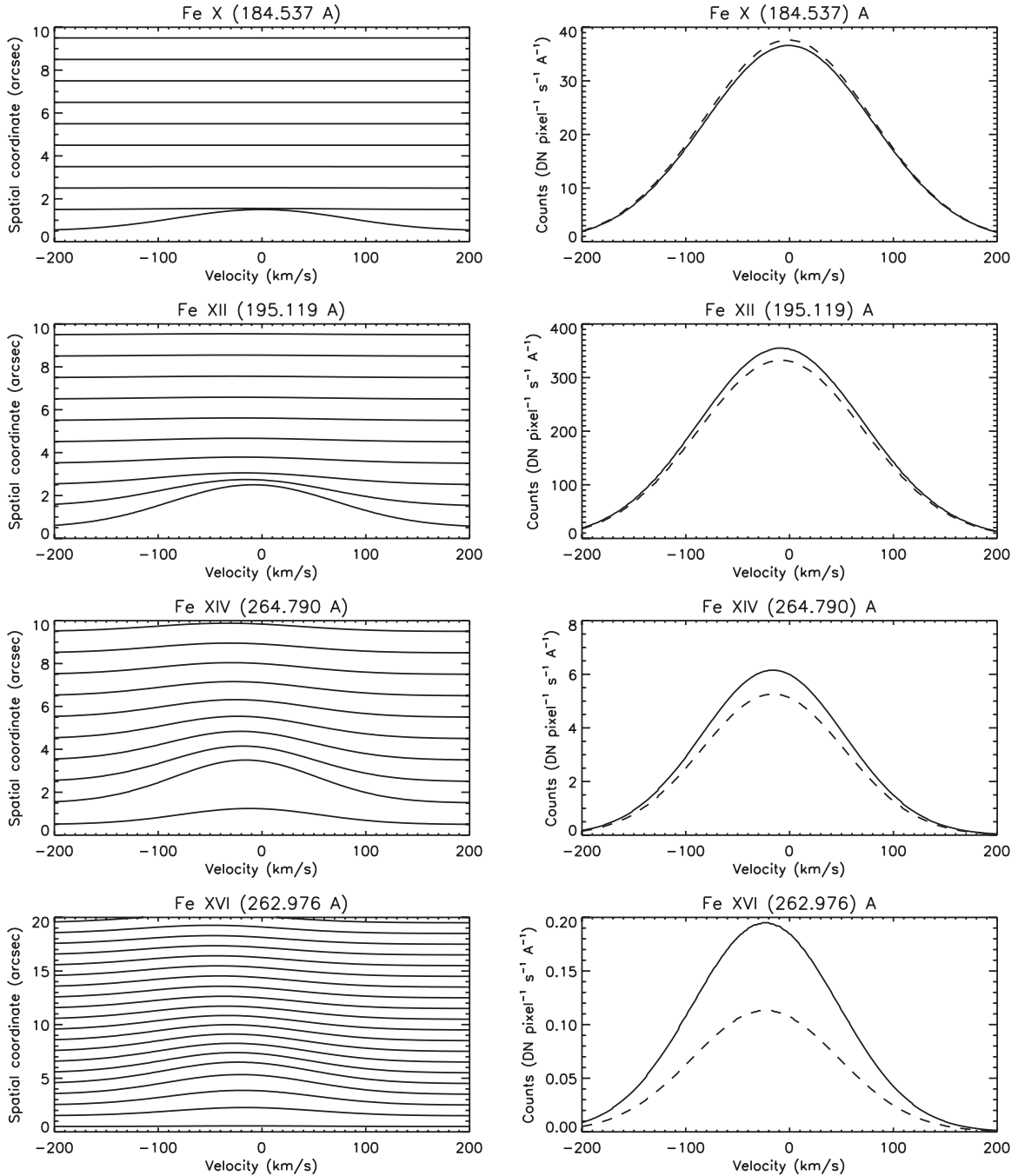


Figure 5. Left-hand column: stack plots showing the Doppler-shift in several coronal emission lines as a function of position along a row of EIS pixels. Right-hand column: line profiles from the pixel of maximum intensity for nonequilibrium (solid) and equilibrium (dashed) ionization.

and denser (near footpoint) regions of the loop, as shown by the Fe X and Fe XII line profiles. In the upper, more rarefied, regions of the loop, higher charge states persist as the rarefaction wave cools the plasma by expansion, leading to a factor of two overpopulation of Fe XVI relative to equilibrium. Hence, nonequilibrium ionization is clearly important in this case.

The Fe XII line at 195.119 Å is by far the strongest and comparing the forward-modeled line profile in Figure 5 with the left-hand plot (Fe XII b) in Figure 1 of Del Zanna et al. (2011), we find excellent agreement between the predicted and observed blueshifts of 10 km s⁻¹ and full width at half-maximum (FWHM) of 83 mÅ. There are also no discernible deviations

from symmetry for the predicted and observed line profiles. The predicted Fe XII intensity at 195.119 Å is approximately half of the observed intensity reported in the blueshifted region by Del Zanna et al. (2011), which is encouraging. The forward-modeling predicts very low counts in the hotter lines, consistent with observations. A detailed comparison with observations is not trivial because of the difficulty in estimating projection effects and we intend to address this issue in a future paper. We believe that our result is satisfactory as it stands and we conclude that the scenario proposed by Del Zanna et al. (2011) leads to upflows in closed coronal loops that are broadly consistent with the properties of the observed flows.

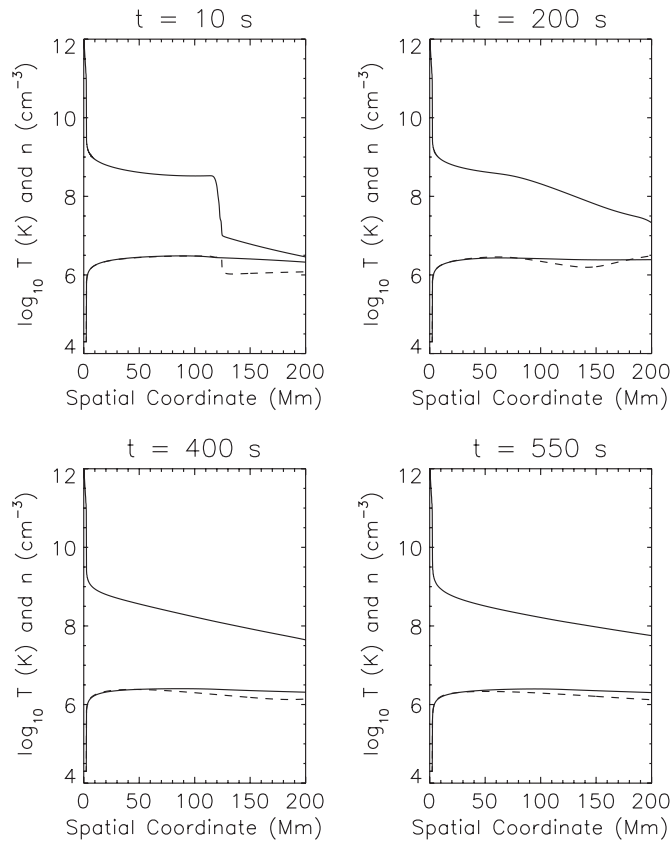


Figure 6. Field-aligned temperature and density profiles at selected times during the development of the rarefaction wave in the open field case. Number density (solid), electron temperature (solid), and ion temperature (dashed).

3.2. Open Field

Figure 6 shows the post-reconnection evolution of the field-aligned number density, electron and ion temperatures for the open field case. It can be seen that even after 550 s the electron and ion temperatures have not collisionally equilibrated. The density and temperature profiles at 400 s and 550 s suggest that the discrepancy between T_e and T_i increases with altitude. Furthermore, our results show that $T_i < T_e$ in the inner corona, as observed for the slow solar wind ($T_i \gg T_e$ in the fast solar wind). Figure 7 shows the evolution of the field-aligned velocity and Mach number. The velocity structure is that of a rarefaction wave and we consider it fully developed by the time it reaches the left-hand footpoint at $t = 550$ s. Therefore, our numerical experiment confirms the development of a rarefaction wave, along the open field line, in the scenario proposed by Del Zanna et al. (2011). Movies of Figures 6 and 7 are available from the authors.

We may eliminate the possibility that this solution corresponds to the unphysical wind discussed in Section 2 because the outflow speed is supersonic ($M \approx 1.3$) at the top of the domain. The lower corona is then isolated from the upper boundary and cannot be affected by sound waves propagating back into the domain. We may now explain why $T_i < T_e$ in the slow solar wind, within the framework of our model. The differential expansion of the plasma along the loop by the rarefaction wave leads to a nearly adiabatic cooling of the ions. But the more efficient transport of energy from the lower atmosphere by electron thermal conduction maintains the electrons at a higher temperature than the ions, for which thermal conduction is significantly less

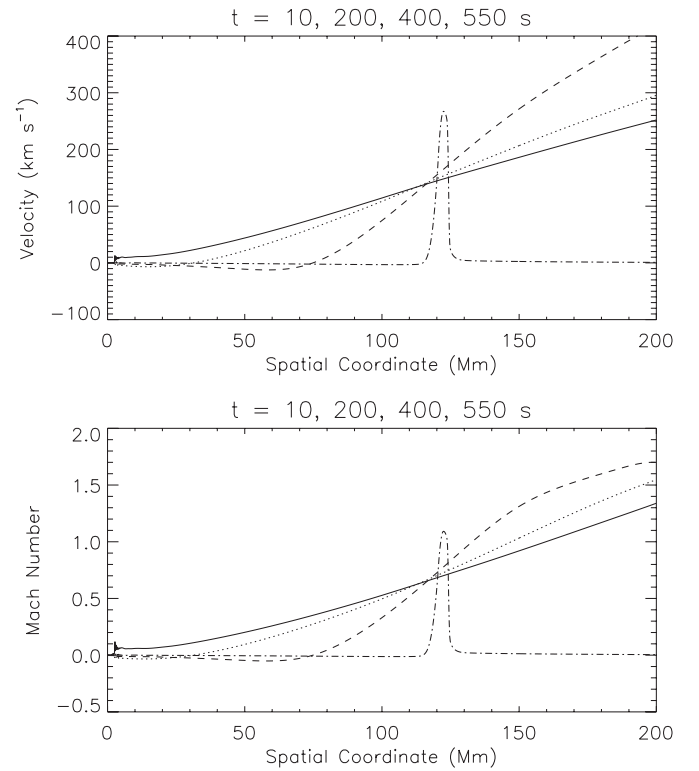


Figure 7. Field-aligned velocity and Mach number profiles at selected times during the development of the rarefaction wave in the open field case. 10 s (dash-dotted), 200 s (dashed), 400 s (dotted), and 550 s (solid).

efficient. The low densities lead to long equilibration timescales and so $T_i < T_e$ persists.

We now determine the spectral properties of the rarefaction wave along the open field line by predicting how such a wave would be observed by *Hinode*-EIS. We assume a viewing geometry such that the instrument line of sight lies directly along the open field line emanating radially outward from the Sun. The emission along the field for each spectral line is then binned into a single EIS pixel and so the spectrum is the line-of-sight integrated spectrum. The line-of-sight depth is equal to the length of the computational domain (200 Mm = 200,000 km). The forward-modeling is carried out on the profiles of the fully developed rarefaction wave at $t = 550$ s in Figures 6 and 7.

Figure 8 shows the line-of-sight integrated spectral line profile and EIS count rates (instrument units) for the open field line. The line profiles show that the outflow speed increases with temperature since the blueshift is greater for higher charge states of Fe. Outflow speeds of 10 km s^{-1} are predicted for Fe x and Fe xii, 20 km s^{-1} for Fe xiv and $40\text{--}50 \text{ km s}^{-1}$ for Fe xvi. The outflow speeds are generally greater than in the closed loop case, due in part to the curvature of the closed loop introducing a $\cos \theta$ effect to the magnitude of the line-of-sight velocity component (where θ is the angle between the field and the line of sight). The spectral line profiles have been plotted for equilibrium and nonequilibrium ionization states to determine what impact this may have on the line intensities. At $t = 550$ s the ionization state is closer to equilibrium for lower charge states (e.g., Fe x and Fe xii). The cooler, denser (hence more collisional) layers of the atmosphere at low altitude make the dominant contribution to the spectral signature of these ions. The nonequilibrium Fe xii and Fe xiv line profiles are slightly redshifted relative to the equilibrium profiles, which indicates a

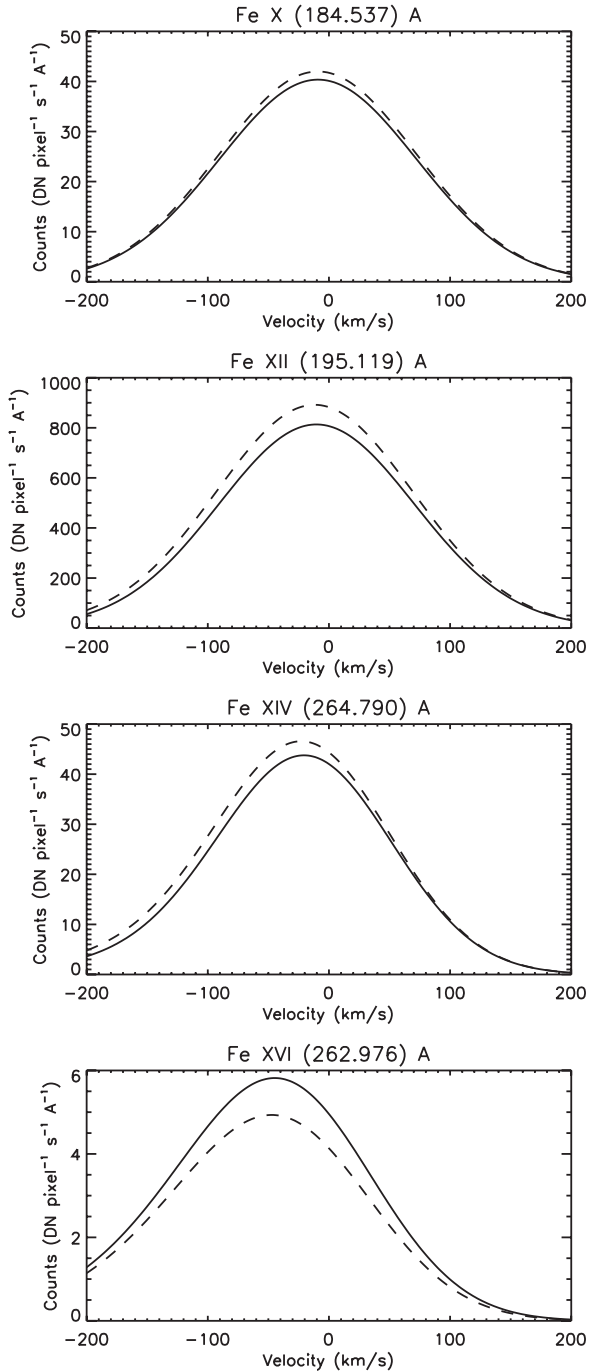


Figure 8. Spectral line profiles in the open field case for nonequilibrium (solid) and equilibrium (dashed) ionization.

small overpopulation of these ions in lower velocity regions of the rarefaction wave. In common with the closed loop case there is an overpopulation of Fe XVI relative to equilibrium, which indicates that the rarefaction expansion cools the plasma and the lack of collisionality allows highly charged ions to persist.

We again find excellent agreement between the predicted (Figure 8) and observed (Fe XII b in Figure 1 of Del Zanna et al. 2011) blueshifts and FWHM, with line profiles that are predicted to be symmetric. Therefore, the contributions to the line-of-sight integrated spectral profile from the high altitude regions of the rarefaction wave, where $v > 100 \text{ km s}^{-1}$, are negligible. The predicted intensity is somewhat greater than the observed

intensity, most likely due to overestimating the line-of-sight depth in our chosen field geometry which, again, arises from the difficulty of accounting for projection effects. Our results indicate that it would be difficult to distinguish between open and closed field regions purely from emission by lower charge states in the interchange reconnection scenario, given the near identical spectral line profiles of Fe X and Fe XII in Figures 5 and 8. Encouragingly, we predict clear differences between the spectral line profiles of higher charge states in open and closed field regions (e.g., stronger blueshifts in open field regions). We conclude that the scenario proposed by Del Zanna et al. (2011) leads to outflows along open field lines at AR/coronal hole boundaries that are broadly consistent with observations.

4. SUMMARY AND CONCLUSIONS

We have conducted numerical experiments in order to determine whether interchange reconnection, as proposed by Del Zanna et al. (2011), can explain the outflows observed as blueshifts in coronal emission lines at open/closed field boundaries. We used a 1D hydrodynamic code to solve for the evolution of the number density, electron and ion temperatures, bulk flow velocity and ionization state, in the case of a strong, post-reconnection pressure gradient in the field-aligned direction. The pressure gradient arises when dense, hot, core loops reconnect with neighboring tenuous, cool, open field lines at high altitude coronal null points. We investigated the post-reconnection open field and closed loop components, and used our numerical results to forward-model the spectral line profiles for a selection of coronal emission lines in order to predict the spectral signatures of flows arising from the interchange reconnection mechanism as they would be observed by *Hinode*-EIS. In both the open field and closed loop cases, we confirm the development of a rarefaction wave consistent with the observed velocity versus temperature structure of the outflow regions. We also note that this model is not inconsistent with the patchy outflows seen by imaging instruments. For example, a single reconnection event can be patchy through island formation by tearing modes (Bárta et al. 2011; Cassak & Shay 2011; Shibata & Tanuma 2001) and even for sequential reconnection in the absence of tearing modes, the AR core loops may have different field strengths, densities, and heating rates which, when the resulting emission is integrated along the line of sight, could lead to the observation of unsteady outflows.

We find a general increase of the outflow speed with emission line formation temperature, and excellent agreement between the predicted and observed spectral line profile of the Fe XII 195.119 Å line in terms of Doppler-shift, FWHM, and symmetry. A detailed comparison with additional observational data will be reported in a future paper. Concerning the symmetrical nature of the line profiles, this may be a reflection of the smooth nature of the rarefaction wave and the plasma that it propagates into. In the case of strongly non-monotonic, field-aligned temperature and density profiles, it may be reasonable to expect significant asymmetries to arise in the line profiles. The structure and field-line geometry of the lower atmosphere is similar for the post-reconnection open and closed field regions, which explains the agreement between the Fe X and Fe XII spectral line profiles in these cases. At higher altitudes significant differences in the atmosphere structure/geometry emerge and these manifest as stronger blueshifts, hence greater outflow speeds, in emission lines from more highly charged coronal ions (Fe XIV and Fe XVI). Finally, we find that $T_i < T_e$ in the inner corona as collision timescales increase. This indicates that the

interchange reconnection scenario we have explored provides a viable mechanism for driving the slow solar wind emanating from ARs.

We believe that our work may profitably be extended by exploring the influence of MHD-related effects; for example, the possibility of magnetosonic shocks and Ohmic heating as the field relaxes during the post-reconnection phase. An important question is whether these are merely transient effects embedded in an overall monotonic, pressure-driven velocity structure, or whether they significantly alter the evolution of the rarefaction wave. Another important question relates to the effect of any expansion of the magnetic field in the corona. Overall, however, we believe that our results constitute strong evidence that interchange reconnection leading to a pressure-driven rarefaction wave can explain the outflows observed in coronal emission lines at open/closed field boundaries.

Financial support by the European Commission through the SOLAIRE Network (MTRN-CT-2006-035484) is gratefully acknowledged by G.A. G.D.Z. acknowledges support from the UK STFC via the Advanced Fellowship programme.

REFERENCES

- Baker, D., van Driel-Gesztelyi, L., Mandrini, C. H., Démoulin, P., & Murray, M. J. 2009, *ApJ*, **705**, 926
- Bárta, M., Büchner, J., Karlický, M., & Kotrč, P. 2011, *ApJ*, **730**, 47
- Bradshaw, S. J., & Klimchuk, J. A. 2011, *ApJS*, **194**, 26
- Brooks, D. H., & Warren, H. P. 2011, *ApJ*, **727**, L13
- Cassak, P. A., & Shay, M. A. 2011, *Space Sci. Rev.*, 110
- Centrella, J., & Wilson, J. R. 1984, *ApJS*, **54**, 229
- Del Zanna, G. 2007, in ASP Conf. Ser. 397, First Science Results from Hinode, ed. S. A. Matthews, J. M. Davis, & L. K. Harra (San Francisco, CA: ASP), 87
- Del Zanna, G. 2008, *A&A*, **481**, L69
- Del Zanna, G., Aulanier, G., Klein, K.-L., & Török, T. 2011, *A&A*, **526**, 137
- Del Zanna, G., & Bradshaw, S. J. 2009, in ASP Conf. Ser. 415, The Second Hinode Science Meeting: Beyond Discovery, Toward Understanding, ed. B. Lites, M. Cheung, T. Magara, J. Mariska, & K. Reeves (San Francisco, CA: ASP), 264
- Del Zanna, L., Velli, M., & Londrillo, P. 1998, *A&A*, **330**, L13
- Doschek, G. A., Warren, H. P., Mariska, J. T., et al. 2008, *ApJ*, **686**, 1362
- Doschek, G. A., Mariska, J. T., Warren, H. P., et al. 2007, *ApJ*, **667**, L109
- Hara, H., Watanabe, T., Harra, L. K., et al. 2008, *ApJ*, **678**, L67
- Harra, L. K., Sakao, T., Mandrini, C. H., et al. 2008, *ApJ*, **676**, L147
- MacNeice, P., Olson, K. M., Mobarry, C., de Fainchtein, R., & Packer, C. 2000, *Comput. Phys. Commun.*, **126**, 330
- Marsch, E., Tian, H., Sun, J., Curdt, W., & Wiegmann, T. 2008, *ApJ*, **685**, 1262
- Parker, E. N. 1958, *ApJ*, **128**, 664
- Schrijver, C. J., Title, A. M., Berger, T. E., et al. 1999, *Sol. Phys.*, **187**, 261
- Shibata, K., & Tanuma, S. 2001, *Earth Planets Space*, **53**, 473
- Taroyan, Y., Bradshaw, S. J., & Doyle, J. G. 2006, *A&A*, **446**, 315
- van Leer, B. 1979, *J. Comput. Phys.*, **32**, 101
- Velli, M. 1994, *ApJ*, **432**, L55
- Verwichte, E., Marsh, M., Foullon, C., et al. 2010, *ApJ*, **724**, L194
- Wang, T. J., Ofman, L., & Davila, J. M. 2011, arXiv:1101.6017v1
- Warren, H. P., Ugarte-Urra, I., Young, P. R., & Stenborg, G. 2011, *ApJ*, **727**, 58
- Winebarger, A. R., DeLuca, E. E., & Golub, L. 2001, *ApJ*, **553**, L81